Solar harvesting based on perfect absorbing all-dielectric nanoresonators on a mirror

Research Article | Vol. 27, No. 16 | 5 Aug 2019 | OPTICS EXPRESS A967
Optics EXPRESS

Solar harvesting based on perfect absorbing all-dielectric nanoresonators on a mirror

ROBIN VISMARA,[1,3,4] NILS ODEBO LÄNK,[2,3] RUGGERO VERRE,[2,5] MIKAEL KÄLL,[2] OLINDO ISABELLA,[1] AND MIRO ZEMAN[1]

[1] *Delft University of Technology, Photovoltaic Materials and Devices Group, 2628CD Delft, The Netherlands*
[2] *Chalmers University of Technology, Department of Physics, 41296 Göteborg, Sweden*
[3] *These authors contributed equally to this work*
[4] *r.vismara@tudelft.nl*
[5] *ruggero.verre@chalmers.se*

Abstract: The high-index all-dielectric nanoantenna system is a platform recently used for multiple applications, from metalenses to light management. These systems usually exhibit low absorption/scattering ratios and are not efficient photon harvesters. Nevertheless, by exploiting far-field interference, all-dielectric nanostructures can be engineered to achieve near-perfect absorption in specific wavelength ranges. Here, we propose – based on electrodynamics simulations – that a metasurface composed of an array of hydrogenated amorphous silicon nanoparticles on a mirror can achieve nearly complete light absorption close to the bandgap. We apply this concept to a realistic device, predicting a boost of optical performance of thin-film solar cells made of such nanostructures. In the proposed device, high-index dielectric nanoparticles act not only as nanoatennas able to concentrate light but also as the solar cell active medium, contacted at its top and bottom by transparent electrodes. By optimization of the exact geometrical parameters, we predict a system that could achieve initial conversion efficiency values well beyond 9% – using only the equivalent of a 75-nm thick active material. The device absorption enhancement is 50% compared to an unstructured device in the 400 nm – 550 nm range and more than 300% in the 650 nm – 700 nm spectral region. We demonstrate that such large values are related to the metasurface properties and to the perfect absorption mechanism.

1. Introduction

Nanoparticles made of high-permittivity materials have attracted extreme interest in the context of nanophotonics. These systems support multipolar geometrical Mie-like resonances and act as nanoantennas, with electric and magnetic field enhancement within their volume. These characteristics make all-dielectric nanoparticles a perfect platform for multiple applications, such as lasing, metamaterials, flat lenses and photon up-conversion to name a few [1–7]. At the same time, all-dielectric nanoantennas are often associated with low Ohmic losses and a clear connection with light harvesting and solar cells has not yet been drawn: these research fields have not yet strongly interacted.

The development of highly efficient thin-film silicon solar cells generally depends on approaches aimed at maximizing the path length of light inside the absorber, which allow for the use of thinner layers, reducing material cost and – in the case of amorphous silicon – the effects of light-induced degradation [8–10]. State-of-the-art thin-film silicon devices rely on random [11–13] or periodic [14, 15] textured substrates/superstrates to efficiently scatter light, thus increasing absorption in the active layer of the solar cell. In single-junction configuration with hydrogenated amorphous silicon (a-Si:H) as active layer, stabilized efficiencies up to 10.2% are achieved – using a commercially available randomly-textured Sn_2O-coated glass (Asahi-VU) as superstrate [11, 12]. The performance of such devices is largely limited by the bandgap of the active medium –

#362520 https://doi.org/10.1364/OE.27.00A967
Journal © 2019 Received 15 Mar 2019; revised 17 May 2019; accepted 17 May 2019; published 27 Jun 2019

Optics EXPRESS

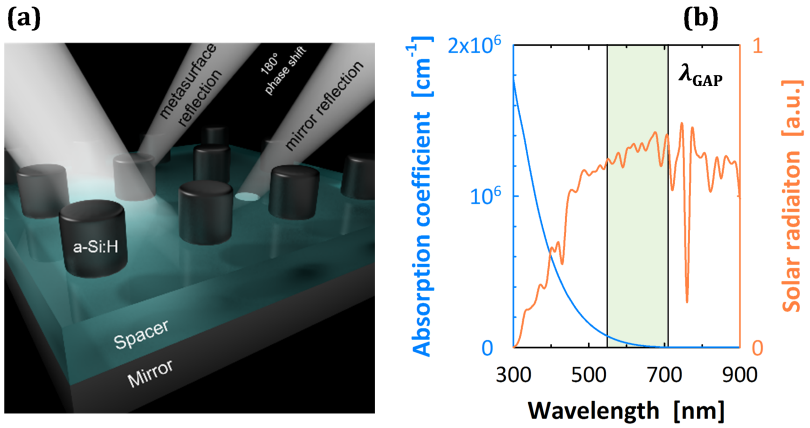

Fig. 1. (a) Sketch of the perfectly absorbing metasurface-on-a-mirror geometry. When the phase difference between metasurface and mirror reflections is 180°, perfect absorption can be achieved. (b) Absorption coefficient of hydrogenated amorphous silicon (blue line) together with the standard AM1.5 solar spectrum radiation (orange line). By engineering the size of the nanoparticles, absorption between 550 nm and 708 nm (green area in b) can be boosted.

$\lambda_{GAP} = 708\,\text{nm} \sim 1.75\,\text{eV}$, Fig. 1(b) – and by weak absorptivity of a-Si:H in the 550 – 708 nm range (i.e. near and up to its bandgap). An alternative route is thus needed to enhance absorption in this part of the spectrum, to better overlap with the solar radiation. A possible solution relies on light trapping and consequent absorption enhancement through surface modulation [16] or periodic nanostructuring [17–23]. For solar cells based on a-Si:H, initial efficiencies up to 10.2% and 9.7% have been obtained, respectively [21, 24, 25].

Nanostructures made of all-dielectric nanoantennas have also been proposed and used to boost and improve the efficiency of different types of solar cell [26–28], but they have been mostly used as scatterers to increase the optical path length inside the absorbing material, or as anti-reflection coatings. An alternative approach is to boost absorption inside the nanoantennas themselves and harvest the generated electron-hole pairs. Despite all-dielectric nanoantennas generally showing small absorption cross-sections in the red region of the visible spectrum, far-field interference effects could be used to increase their absorption. This effect could in theory be used for photon harvesting. In particular, if particles are arranged in a metasurface fashion, it is possible to reach complete absorption in specific wavelength ranges [29]. In the past few years, several studies on perfect absorbers have been reported, both for plasmonic and all-dielectric nanoantennas, and the phenomenon has been used for phase-based sensing [30, 31], terahertz absorption [32], strong coupling [33], light harvesting [2, 34], and photocatalysis [35].

In this article, we propose a novel type of solar cell where the concept of perfect absorption in a particle-on-a-mirror geometry is employed to boost the efficiency of a-Si:H thin film solar cells. The system under study consists of all-dielectric nanoparticle (nanodisk) arrays arranged in a metasurface-like fashion and placed atop a thick mirror. In this configuration, sketched in Fig. 1(a), the mirror clearly prevents transmission. At the same time, the relative reflection phase difference between the mirror and the metasurface can be controlled by varying the spacing between the two. If the spacing and the particle geometry are chosen such that (i) the relative phase shift between metasurface and mirror reflections is 180° and (ii) the respective amplitude is the same, reflection is suppressed and 100% absorption inside the dielectric particles can be achieved, at specific wavelengths. By careful design of the metasurface properties, resonant absorption enhancement can thus be tuned to the spectral region where the intrinsic a-Si:H absorption is

Optics EXPRESS

low – green region in Fig. 1(b) but the solar spectrum still contains significant energy. By contacting the a-Si:H nanodisks at top and bottom, electron-hole pairs that are generated inside the nanoparticles can be harvested. The concept of perfect absorption based on interference has been used in a number of systems composed of plasmonic or semiconductor particles or gratings [36, 37]. However, up to date, harvesting the generated electron-hole pairs for photon harvesting applications still remains the main concern. In this respect, the proposed structure should not pose particular challenges when it comes to contacting, and surface recombination is not expected to be an issue since the particles are embedded in a silicon-oxide layer – a material commonly and effectively used to passivate silicon photovoltaic devices [38–41]. In this way, issues of recombination and contacting commonly found in nanostructured solar cells can be avoided.

In this work, after analyzing the simple case of a nanostructured metasurface on a mirror, we propose a real device and optimize its geometrical properties *via* a rigourous 3D Maxwell equation solver using experimentally-determined permittivity data. We predict a photocurrent density $J_{\mathrm{ph}} > 14\,\mathrm{mAcm}^{-2}$ using 300-nm tall disks. This corresponds to a theoretical efficiency beyond 9.5% for an equivalent active material thickness < 75 nm. The predicted photocurrent value represents an enhancement of > 3 times with respect to absorption in thick flat layer with the same total 300nm thickness in the 650 nm – 708 nm part of the spectrum, i.e. in the region where the perfect absorption mechanism was optimized.

2. Methodology

2.1. Finite-difference time-domain particle-on-a-mirror simulations

The FDTD simulations for the metasurface-on-a-mirror system in Fig. 2 were performed using FDTD Solutions (Lumerical Inc., Canada, [42]). The nanoparticle was modeled as a cylindrical a-Si:H structure with $D = 140\,\mathrm{nm}$ and $h = 300\,\mathrm{nm}$, while the metasurface arrangement was accomplished using periodic boundary conditions with a periodicity of $P = 250\,\mathrm{nm}$ for Fig. 2(c) and $145\,\mathrm{nm} < P < 350\,\mathrm{nm}$ for Fig. 2(d). The nanodisks were embedded in a dielectric medium with the refractive index of SiO_2 ($n_s = 1.46$). A semi-infinite silver substrate was placed at varying distances below the nanoparticles: $5\,\mathrm{nm} < d_s < 500\,\mathrm{nm}$ for Fig. 2(c) and fixed at $d_s = 100\,\mathrm{nm}$ for Fig. 2(d). Thus, in this model, the spacer between the metasurface and the mirror has the same refractive index as the embedding medium ($n_s = 1.46$). The meshing employed on the nanostructure was $\mathrm{d}x = \mathrm{d}y = \mathrm{d}z = 2\,\mathrm{nm}$, which was deemed sufficient to capture the spatial variation of the electromagnetic modes considered in this work. The (complex) dielectric functions used were fitted to experimental data for both a-Si:H (internally measured) and the silver mirror [43]. Absorption in a-Si:H – Figs. 2(c) and 2(d) was calculated by integrating the total Poynting vector flow through a closed boundary enclosing the particle and normalized by the injected plane wave power. The surface was placed such that it did not intersect the mirror surface. Thus, the total integrated power flux through that surface corresponds exactly to the power absorbed by the nanostructure.

2.2. Multipole decomposition

The multipole decomposition of the modes was performed by monitoring the internal electromagnetic fields in the nanostructure, as function of the wavelength of light. The fields were then projected on a basis of spherical multipoles as outlined in [44]. The electric fields were converted into polarization current according to

$$\mathbf{J} = -i\omega\varepsilon_0[\varepsilon_{\text{a-Si:H}}(\omega) - n_s^2]\mathbf{E}\,, \tag{1}$$

where $\mathbf{E}$ is the total electric field inside the structure. Since the fields in the simulations (both the FDTD simulations and the FEM simulations) were defined on a Cartesian grid, the conversion to

spherical coordinates was made through:

$$\begin{aligned} J_r &= \sin(\vartheta)\cos(\phi)J_x + \sin(\vartheta)\sin(\phi)J_y + \cos(\vartheta)J_z \,, \\ J_\vartheta &= \cos(\vartheta)\cos(\phi)J_x + \cos(\vartheta)\sin(\phi)J_y - \sin(\vartheta)J_z \,, \\ J_\phi &= -\sin(\phi)J_x + \cos(\phi)J_y \,. \end{aligned} \tag{2}$$

The multipole decomposition was subsequently calculated through integration on the Cartesian grid, and the coefficients here relate to those in Eqs. (15) and (16) in [44] as

$$|a_\ell|^2 = (2\ell+1)\sum_{m=-\ell}^{\ell} |a_E(\ell,m)|^2 \,, \qquad |b_\ell|^2 = (2\ell+1)\sum_{m=-\ell}^{\ell} |a_M(\ell,m)|^2 \,. \tag{3}$$

2.3. Finite element method device simulation

Device simulations were conducted using ANSYS's High Frequency Structure Simulator (HFSS), a 3-dimensional Maxwell equation solver based on the Finite Element Method (FEM) [45]. The software allows for the accurate modelling of thin-film solar cell structures with arbitrarily complex geometries [46,47], provided that the input optical properties (wavelength dependent refractive index, n and extinction coefficient, κ) of all materials are accurately characterized [48,49]. The intensity of the electric field, obtained from the solution of the Maxwell equations, is used to calculate the absorption of the device:

$$A_i = \frac{1}{2}\varepsilon_0 \,\mathrm{Im}(\varepsilon_i)\,\omega \int_{V_i} |\mathbf{E}(x,y,z)|^2 \,\mathrm{d}V \,, \tag{4}$$

where A_i is the absorption in the i^{th} layer of the solar cell and ε_0 the permittivity of vacuum. Here, ε_i is the relative permittivity of the i^{th} layer, ω is the angular frequency of light and (x, y, z) denote the coordinates inside the i^{th} layer of volume V_i. Note that the wavelength (λ) dependence of A_i, ε_i, ω and $\mathbf{E}$ is not explicitly indicated. Reflection is computed from S-parameters (i.e. elements of the scattering matrix $\mathbf{S}$) as $R = |s_{11}|^2$. The integral – over the investigated spectrum – of the product of $A_i(\lambda)$ or $R(\lambda)$ and the photon flux of the standard AM1.5 solar spectrum $\Phi_{\text{AM1.5}}(\lambda)$ [50] yields the implied photocurrent density generated (in the absorber) or lost (in supporting layers or due to reflection):

$$J_{\text{ph-}i} = |q| \int_{\lambda=300\,\text{nm}}^{\lambda=900\,\text{nm}} X(\lambda)\Phi_{\text{AM1.5}}(\lambda)\,\mathrm{d}\lambda \,, \tag{5}$$

where $|q| = 1.602 \times 10^{-19}\,\text{C}$ is the elementary charge, and $X(\lambda)$ can either be $A_i(\lambda)$ or $R(\lambda)$. Note that – in this work – only the spectral range $300\,\text{nm} < \lambda < 900\,\text{nm}$ has been considered.

3. Results

3.1. Perfect absorption in a particle-on-a-mirror geometry

To illustrate the concept of perfect absorption in a particle-on-a-mirror geometry the simplest case possible was chosen, i.e. a periodic array of a-Si:H nanodisks on top of an infinite Ag mirror, separated by a glass spacer with thickness d_s and refractive index $n_s = 1.46$ – c.f. sketch in Fig. 1(a). We first modelled the particle-on-a-mirror metasurface using FDTD methods [42]). The nanodisks have a fixed height ($h = 300\,\text{nm}$) and diameter ($D = 140\,\text{nm}$), and are arranged in a square lattice configuration with period of $P = 250\,\text{nm}$. For this value of the periodicity the a-Si:H array essentially acts as a metasurface, since the distances and dimensions considered are much smaller than the incident wavelength (no diffuse scattering is present). Optical absorption in the nanodisk was calculated by integrating the Poynting vector on a surface enclosing the

Optics EXPRESS

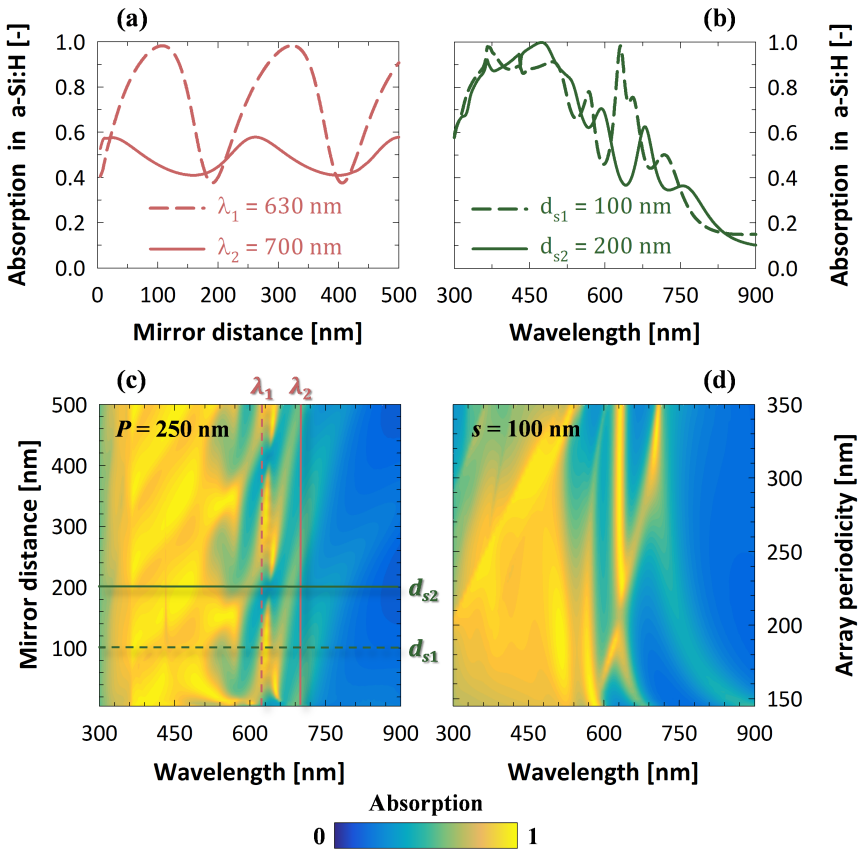

Fig. 2. (a) Absorption in a-Si:H as function of the distance from the mirror, at $\lambda_1 = 630\,\text{nm}$ and $\lambda_2 = 700\,\text{nm}$. (b) Absorption spectra for two specific mirror distances, $d_{s1} = 100\,\text{nm}$ and $d_{s2} = 200\,\text{nm}$. (c) Absorption spectra as a function of mirror distance, for $P = 250\,\text{nm}$. The vertical (red) and horizontal (green) colored lines are related to the data shown in (a) and (b), respectively. (d) Absorption spectra as a function of the array periodicity, for $d_s = 100\,\text{nm}$.

particle, but excluding the mirror (see Methodology for details). Light absorption in the active material was thus decoupled from all other loss channels, such as any surface plasmons excited on the mirror interface or other absorption in the silver. It was also verified that most (98%) of the total absorption took place inside the metasurface, rather than in the silver mirror.

In Fig. 2(a), the absorption amplitude for this system at $\lambda_1 = 630\,\text{nm}$ and $\lambda_2 = 700\,\text{nm}$ is shown, as function of the mirror distance d_s. The amplitudes oscillate with a period $\Lambda_i = \lambda_i/(2n_s) = 210\,\text{nm}$ and 233 nm, respectively (where $i = 1, 2$). The differences in the period of oscillations can be simply understood as a Fabry-Perót like resonance, as the system setup is analogous to a Salisbury screen perfect absorber [51] for specific wavelengths. Absorption in such a screen is maximized when $d_s = \lambda/(4n_s)$, i.e. when the reflections present 180° phase difference. Indeed, for $\lambda_1 = 630\,\text{nm}$ a maximum in absorption can be observed at $d_s = 105\,\text{nm}$ – see Fig. 2(a).

Interestingly, reflection and absorption at specific wavelengths (630 nm with the present nanodisk dimensions) can thus be modulated from 40% to 100%, by simply modifying the spacer thickness. Fabry-Perót oscillations can also be seen in the absorption spectra *versus* wavelength,

for fixed spacing of the mirror – see Fig. 2(b). In this case, however, they are modulating the resonant behavior of the Si nanodisk array. The full absorption spectral dependence on the mirror distance is shown in Fig. 2(c). The system response for varying array periods was also studied – keeping the spacer distance constant at $d_{s1} = 100\,\text{nm}$. Absorption as function of the period P – Fig. 2(d) shows a rich dispersion and coupling of various modes. The data confirms that the overall absorption is decreased at larger periodicities – as less active material is present – and that the diffractive modes appear in the region of high absorption, i.e. 300 nm – 500 nm, i.e. where $\lambda \approx n_s P$.

3.2. Design of an a-Si:H solar cell based on perfect absorption

So far, we have demonstrated that it is possible to achieve enhanced absorption in the very simple case of a-Si:H nanodisks on top of a mirror, owing to Fabry-Perót like interference effects between the a-Si:H layer and mirror reflections. Shifting our attention to calculations of a realistic device, we propose a nanophotonic metasurface consisting of a-Si:H nanodisks embedded in a transparent lossless dielectric medium (SiO_2). The nanostructures have a fixed height of 300 nm. The particle diameter (D) and the period of the array (P) were varied in the ranges $D = 80 - 240\,\text{nm}$ and $P = 100 - 500\,\text{nm}$, respectively. A commercially available 3D Maxwell equation solver based on the finite element method (FEM) [45] was employed to model the entire device structure.

A 20 nm thick (boron-) phosphorous-doped nanocrystalline silicon oxide (nc-SiO_x:H) layer is added on the (top) bottom of the absorber, to create an electric field that separates the photo-generated charge carriers (electrons, e^- and holes, h^+). The charge carriers are then collected on opposite sides: e^- at the negative, n-contact and h^+ at the positive, p-contact. At the front side (p-contact, top), a highly transparent conductive oxide (TCO) is selected, In_2O_3:H (IOH, thickness: 100 nm), thanks to its favorable optoelectrical properties [52, 53]. At the back (n-contact, bottom), a TCO-metal combination of ZnO:Ga (GZO [54]) and silver (Ag) is selected, with thickness of 70 nm and 300 nm, respectively. Both values are typically used in thin-film silicon photovoltaics [55–57]. The presence of GZO between semiconductor and metal improves the reflectivity of the back side, and the thickness was chosen to allow efficient electron collection at the metal contact. At the same time, the GZO layer serves as the spacer for achieving destructive interference between the two reflections, thus maximizing absorption in the SiO_2-filled metasurface. Regarding the p- and n-type layers, two possible configurations can be devised. First, they can be included in the metasurface structure (structure type A), i.e. being a part of the a-Si:H nanodisks on each side. Alternatively, they can be deposited on the entire device area (type B). Both possibilities were considered, and the respective device models are depicted in the insets of Figs. 3(a) and 3(b).

The nanodisks are ordered in a 2D square lattice. However, similar results can be expected using randomly dispersed particles and effective medium theories [29]. In Figs. 3(a) and 3(b), the implied photocurrent density in the absorber ($J_{\text{ph-aSi:H}}$) is shown – as a function of diameter D and periodicity P – for device types A and B. For both configurations, two general trends are observed. First, $J_{\text{ph-aSi:H}}$ increases when the distance between disks is reduced. Second, a better performance is observed for structures with larger diameter. Both effects correlate to the total amount of absorbing material, which increases with both a decrease in P and an increase in D. However, we observe the optimum response at $(P; d) = (250\,\text{nm}; 140\,\text{nm})$ which does not correspond to the maximum amount of absorbing material within the solar cell. It is also interesting to note that, for both configurations, the best performance ($J^{(\text{A})}_{\text{ph,a-Si:H}} = 13.80\,\text{mAcm}^{-2}$ and $J^{(\text{B})}_{\text{ph,a-Si:H}} = 14.14\,\text{mAcm}^{-2}$) is achieved for the same $(P; d)$ pair. In the following, it will be demonstrated that it is the interference between metasurface and mirror reflection that maximizes the solar cell performance. Considering state-of-the-art V_{oc} and FF values of *substrate* [58] and *superstrate* [12] a-Si:H single-junction devices – deploying ~ 250-nm thick absorbers – our

Optics EXPRESS

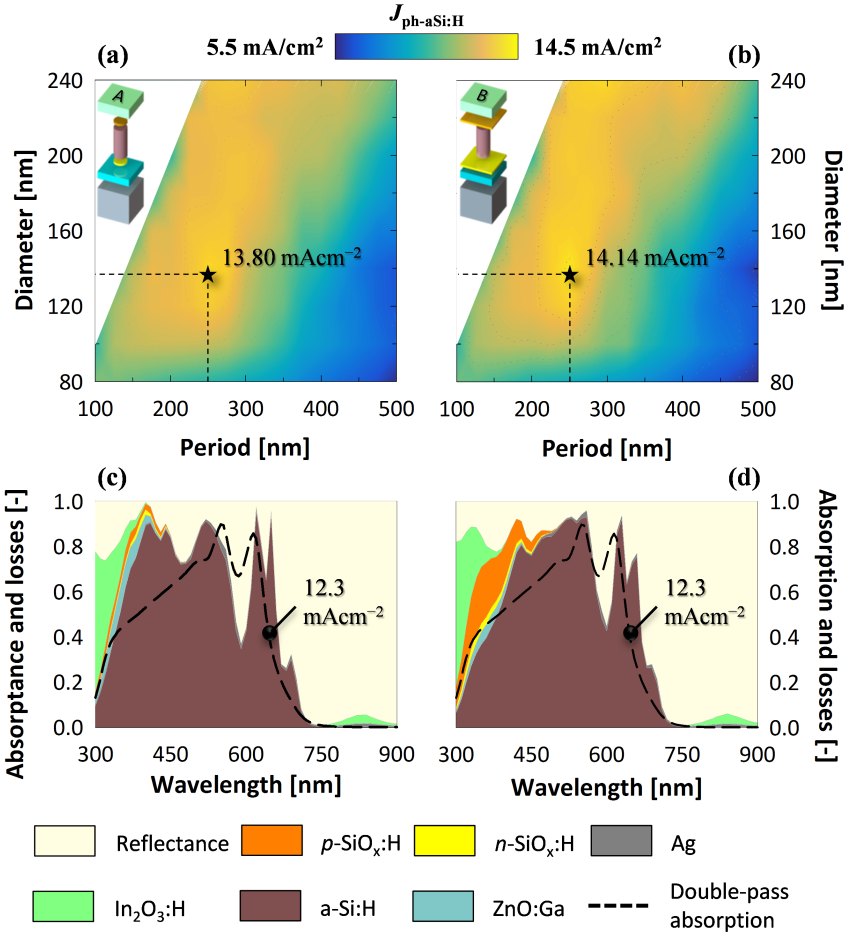

Fig. 3. Implied photocurrent density in the absorber ($J_{ph\text{-}aSi:H}$), as function of nanodisk diameter and distance, for device configurations A (a) and B (b). 3D sketches of the simulation models are included in the insets (note that the SiO_2 filler has not been depicted for clarity). The star symbol corresponds to the parameter combination providing the maximum implied photocurrent. (c-d) Absorption spectra of the different materials in the stack for the most efficient periodicity/diameter combination. The dashed black line indicates absorption in an unstructured layer with the same thickness placed in the same environment.

Optics EXPRESS

calculated best photocurrent densities would imply an initial conversion efficiencies between 8.1% and 9.6 % (for both configurations), albeit for an active material with equivalent thickness < 75 nm. To better outline the different performance between configurations A and B, we analyzed the respective absorption spectra as function of the wavelength λ – Figs. 3(c) and 3(d). In both cases, distinct absorption peaks are observed for $\lambda > 600$ nm. Device model B suffers from higher parasitic absorption losses in the p-type nc-SiO_x:H layer, due to the fact that it covers the entire area rather than only the a-Si:H nanostructures. However, reflection is smaller in the blue range, providing similar overall absorption and efficiency.

It is also instructive to compare the device absorption with a simple unstructured 300 nm thick a-Si:H layer, which is a typical thickness in standard a-Si:H solar cells. The film is sandwiched in the same environment as the metasurface (IOH/*p*/a-Si:H/*n*/GZO/Ag). The thickness of the GZO layer was changed to 40 nm, which was found to be the optimum for the flat reference device. The spectrum, overlayed as a black dashed line in Figs. 3(c) and 3(d) is also helpful to clarify the absorption spectra of the metasurface itself. Fabry-Perót modes – which depend on the layer thickness – appears at around $\lambda = 560$ nm and $\lambda = 620$ nm for both the metasurface and the unstructured layer. However, additional absorption appear both at shorter and at longer wavelength for the metasurface. Close to the band gap, the system presents resonances that concentrate the light within the active medium and increase absorption. The significant metasurface absorption enhancement in the 350 nm – 550 nm is instead related to diminished reflection. This reason is that the particle layer contains roughly four times less a-Si:H than the unstructured layer, and so the effective refractive index of the metasurface is lower ($n_{\mathrm{SiO2}} < n_{\mathrm{meta}} < n_{\mathrm{a\text{-}Si:H}}$). This improved impedance matching between the layers reduces the parasitic reflections in the system and enhances the absorption. The metasurface thus also acts as its own effective anti-reflection coating in this spectral range.

We now turn our attention to the wavelength interval $600\,\mathrm{nm} < \lambda < \lambda_{\mathrm{GAP}} = 708$ nm, where absorption in the metasurface is clearly enhanced compared to a homogeneous a-Si:H film. In order to quantify the resonant absorption enhancement close to the bandgap, a multipolar analysis of the EM field inside the amorphous silicon nanodisks was carried out for the most efficient type A configuration. This allows for identification of the resonant modes excited in the nanodisks. The multipolar response for the different electric and magnetic multipoles is plotted in Fig. 4, for a system without Fig. 4(a) and with Fig. 4(b) mirror at the backside. The internal fields were projected on a spherical multipole basis [44], and the individual particles' mode amplitudes for electric (a_ℓ) and magnetic (b_ℓ) multipoles were calculated (see Methods for details). Note that this decomposition assumes a homogeneous dielectric environment, which is not fulfilled here. A precise decomposition requires knowledge of the Green's function outside the particle. However, the analysis carried out in this work is adequate for the purpose of showing the nature of the modes and the absorption enhancement linked to them.

The decomposition of the internal fields shows a rich resonance structure in the spectral region of interest. In particular, various multipolar responses (electric and magnetic dipoles and quadrupoles) are overlapped. Nevertheless, the response of the nanodisk array is dominated by electric and magnetic dipolar resonances, whose amplitudes are enhanced more than 4 times close to the bandgap once the system is placed on top of the mirror. This behavior is clearly related to scattering suppression due to destructive interference, which increases the lifetime of the modes and thus the absorption. A different, but equivalent, way to see this is by looking at the field enhancement inside the dielectric nanodisks – see Figs. 4(c) and 4(d). Absorption takes place within these a-Si:H nanoantennas and is proportional to $A \propto \mathrm{Im}(\varepsilon_{\mathrm{aSi:H}}) \int |\mathbf{E}(\mathbf{r})|^2 \mathrm{d}V$, where $\mathbf{r}$ is the position within the volume V. Simulations show that the fields are significantly larger inside the nanodisks when a mirror is employed, explaining the enhancement observed in Figs. 4(a) and 4(b).

Figure 4 depicts all multipolar modes that are excited within each nanoantenna. The presence of

Optics EXPRESS

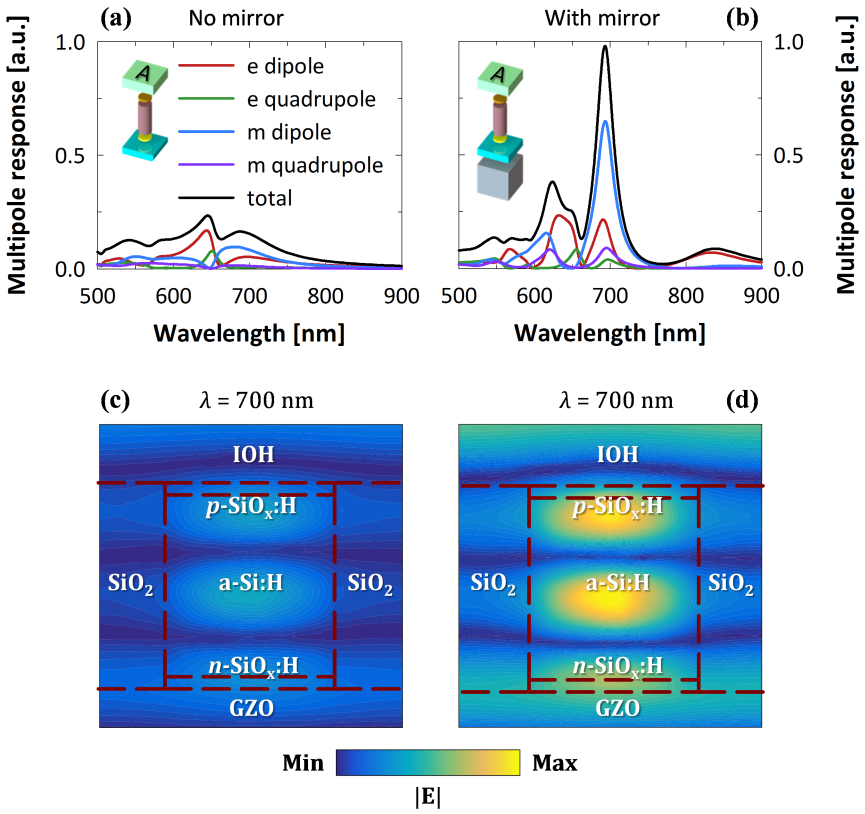

Fig. 4. Multipolar analysis for solar cell (structure A), for parameters corresponding to the maximum implied photocurrent density without (a) and with (b) back-mirror reflector. The mode analysis shows a large increase in the modes amplitudes in the 550 – 700 nm wavelength range, due to interference effect with the mirror. The increase amplitude is accompanied by increased near field distribution inside the nanoparticles, shown in (c) and (d) for the two cases (without and with mirror, respectively) at $\lambda = 700$ nm.

high order spherical harmonic modes overlapped with the dipolar response is due to the complex nature of the structure and the presence in it of highly dispersive layers. Nevertheless, it is possible to study the real modes' pseudo-dispersion by simply plotting absorption spectra as a function of the particle diameters (Fig. 5). For $\lambda < 500$ nm, where the absorptivity of a-Si:H is very high, absorption is clearly almost independent of the diameter D. For $500\,\text{nm} < \lambda < \lambda_{GAP} = 708$ nm, several clear resonances are observed, which disperse almost linearly with the diameter. These peaks in the absorption spectra red-shift when nanodisks with larger diameter are used, at a different rate, providing an additional route to fine tune the absorption and the response of the system. In particular, the geometrical optimum $D = 140$ nm was found to coincide with a balance between the separation between these modes and convoluted with the absorption in a-Si:H.

4. Discussion

From a practical point of view, the particle-on-a-mirror system presented here is possible to fabricate. A simple route would rely on patterning of the nanodisks using self-assembled large scale nanoimprint methods [26, 59], followed by a planarization step and the deposition of the top contact. Due to the departure from full planar deposition, and therefore not dealing with bulk

Optics EXPRESS

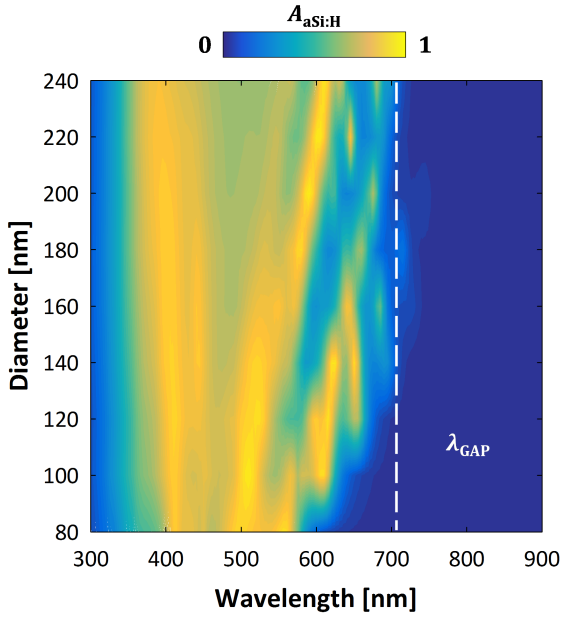

Fig. 5. Absorption spectra in the a-Si:H metasurface, as a function of the particle diameter, for device structure A and $P = 250\,\text{nm}$ ($\lambda_{gap} = 708\,\text{nm}$).

absorbers, it is also expected that such nano-structuring would help in quenching light-induced degradation in thin-film a-Si:H solar cells [10].

The design proposed here is also general in the sense that it can be adapted to other types of solar cell architectures, provided the active material possesses large permittivity values. For example, Mie modes were already shown to be supported by both GaAs [60–62] and perovskite nanoparticles [63, 64]. This means that the particle-on-a-film geometry could be adapted to standard crystalline thin film solar cells as well as thin-film devices based on direct bandgap materials. In fact, the approach detailed in this work might suit such materials even better, owing to their high absorptivity values for larger wavelengths range due to the smaller band-gaps [65,66]. The metasurface geometry and spacer thickness would then need to be optimized accordingly and in different wavelength regions.

Clearly, one of the main limitations of the perfect absorption concept is that it relies on far-field interference and only works at a single wavelength. While in this work we wanted to focus on the lowest energy modes – as they provide a clearer picture for a proof of principle application – current research in all-dielectric nanophotonics aims at realizing, *via* nanostructuring, new eigenmodes [67, 68]. For example, once particles of several hundreds of nm are used, several multipolar resonances appear and can be engineered to overlap. This can broaden the effective optical response of the system, or give rise to unusual response that can boost light-matter interaction even further. Another problem of the particle-on-a-mirror system proposed in this contribution is that the geometry has been optimized for normal incidence (i.e. perpendicular illumination). However, the phase between the different reflections does not strongly depend on the illumination angle; an incident angle of 30° gives a change in phase of around 10% – based on the difference in optical path length: $2d/\cos\vartheta_2$, where ϑ_2 is the angle of refraction. This means that the optimized wavelength of operation of the perfect absorption concept is quite robust to changes in illumination conditions. In fact, this is shown in Fig. 6, where the device absorption spectrum as function of the angle of incidence (AoI) of light is plotted. For $\lambda < 550\,\text{nm}$, it can

Optics EXPRESS

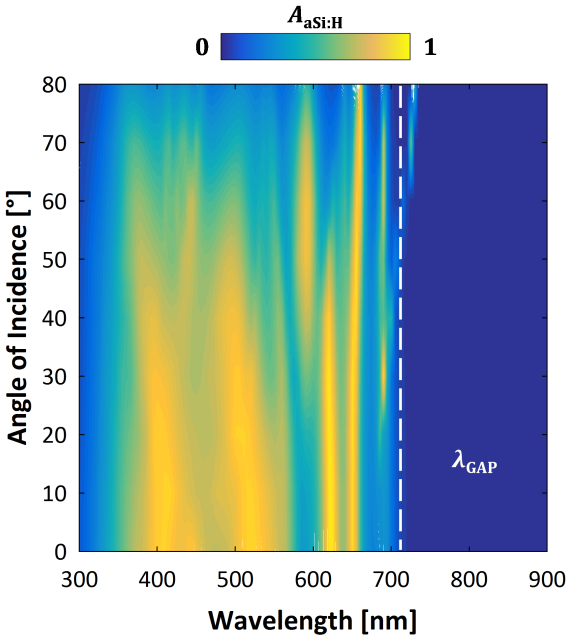

Fig. 6. Absorption spectra inside the a-Si:H layer, as function of the angle of incidence of light.

be observed that absorption is almost constant for values of AoI up to 40°. Only for AoI > 40° a decrease of $A_{aSi:H}$ is observed. Of particular interest is the behavior that can be observed in the spectral region between 550 nm and λ_{gap}. As already depicted in Fig. 3(c), three absorption peaks can be observed: at $\lambda \approx 620$ nm, at $\lambda \approx 650$ nm and at $\lambda \approx 690$ nm. These three peaks are also clearly visible in Fig. 6. While their intensity varies with AoI (except for $\lambda \approx 650$ nm), their position is not affected by the angle of incidence. This indicates that the wavelengths at which confinement of the electromagnetic field within the nanodisks take place – which results in resonances in the absorption spectra – is only dependent on their diameter and distance, as previously shown in Figs. 3 and 5. The global performance, expressed in terms of $J_{ph\text{-}aSi:H}$, remains almost constant for values of AoI up to 40° – $J_{ph\text{-}aSi:H}(\text{AoI} = 40°) = 13.2\,\text{mAcm}^{-2}$. For AoI > 40° the global performance drops significantly, mainly due to increased reflection at the front side of the solar cell. Finally, using the same concept presented here, one could imagine adapting the design to a photo-detector and, owing to the flexibility in the design of all-dielectric nanoantennas, directional, chiral or other types of exotic efficient light harvesters could be envisioned.

5. Conclusions

In this work, we discussed how all-dielectric nanoantennas can be adapted as solar harvesters. The basic idea is that by exploiting far-field interference effects it is possible to increase the absorption in regions were material generally present low absorptivity. We presented here a novel and potentially attractive solar cell structure, employing an all-dielectric silicon metasurface as an active layer in a traditional thin-film silicon solar cell architecture. The nanodisks composing the metasurface can realize perfect (near 100%) absorption at specific wavelengths, due to interference between light reflected by the nanostructures and by the underlying mirror. The operational wavelength can be tuned by changing the system parameters and can boost absorption

near the bandgap of the material, i.e. where the absorption coefficient is generally low. The configuration displaying the best optical performance yields an implied photocurrent density of 14.14 $mAcm^{-2}$, with the potential to achieve initial conversion efficiencies above 9.5%, in line with current state-of-the-art amorphous silicon solar cells which employ significantly thicker absorber layers. An in-depth analysis showed that the optical nanodisks have the multiple function of acting as (i) cavities, trapping the electromagnetic field within, (ii) as the solar cell active medium and (iii) as anti-reflective agents, strongly decreasing parasitic reflection in the blue-green region of the visible spectrum. The perfect absorption concept is also shown to be robust with respect to the angle of incidence of light. These results can thus be considered as a proof-of-principle study where the advantages of all-dielectric nanoantennas have been adapted to develop a solar harvester based on a new concept.

Funding

Knut and Alice Wallenberg Foundation; Swedish Foundation for Strategic Research.

Disclosures

The authors declare that there are no conflicts of interest related to this article.

References

1. L. Cao, J. S. White, J.-S. Park, J. A. Schuller, B. M. Clemens, and M. L. Brongersma, "Engineering light absorption in semiconductor nanowire devices," Nat. Mater. **8**, 643 (2009).
2. H. A. Atwater and A. Polman, "Plasmonics for improved photovoltaic devices," Nat. Mater. **9**, 205 (2010).
3. D. Fattal, J. Li, Z. Peng, M. Fiorentino, and R. G. Beausoleil, "Flat dielectric grating reflectors with focusing abilities," Nat. Photonics **4**, 466 (2010).
4. B. W. H. Baugher, H. O. H. Churchill, Y. Yang, and P. Jarillo-Herrero, "Optoelectronic devices based on electrically tunable p-n diodes in a monolayer dichalcogenide," Nat. Nanotechnol. **9**, 262 (2014).
5. D. Lin, P. Fan, E. Hasman, and M. L. Brongersma, "Dielectric gradient metasurface optical elements," Science **345**, 298 (2014).
6. K. E. Chong, I. Staude, A. James, J. Dominguez, S. Liu, S. Campione, G. S. Subramania, T. S. Luk, M. Decker, D. N. Neshev, I. Brener, and Y. S. Kivshar, "Polarization-independent silicon metadevices for efficient optical wavefront control," Nano Lett. **15**, 5369–5374 (2015).
7. F. Aieta, M. A. Kats, P. Genevet, and F. Capasso, "Multiwavelength achromatic metasurfaces by dispersive phase compensation," Science **347**, 1342 (2015).
8. D. L. Staebler and C. R. Wronski, "Reversible conductivity changes in discharge-produced amorphous si," Appl. Phys. Lett. **31**, 292–294 (1977).
9. D. Staebler and C. R. Wronski, "Optically induced conductivity changes in discharge-produced hydrogenated amorphous silicon," J. Appl. Phys. **51**, 3262–3268 (1980).
10. H. Kakinuma, S. Nishikawa, and T. Watanabe, "Thickness dependence of staebler-wronski effect in a-si: H," J. Non-Crystalline Solids **59**, 421–424 (1983).
11. T. Matsui, K. Maejima, A. Bidiville, H. Sai, T. Koida, T. Suezaki, M. Matsumoto, K. Saito, I. Yoshida, and M. Kondo, "High-efficiency thin-film silicon solar cells realized by integrating stable a-si:h absorbers into improved device design," Jpn. J. Appl. Phys. **54**, 08KB10 (2015).
12. T. Matsui, A. Bidiville, K. Maejima, H. Sai, T. Koida, T. Suezaki, M. Matsumoto, K. Saito, I. Yoshida, and M. Kondo, "High-efficiency amorphous silicon solar cells: Impact of deposition rate on metastability," Appl. Phys. Lett. **106**, 053901 (2015).
13. H. Tan, E. Moulin, F. T. Si, J.-W. Schüttauf, M. Stuckelberger, O. Isabella, F.-J. Haug, C. Ballif, M. Zeman, and A. H. M. Smets, "Highly transparent modulated surface textured front electrodes for high-efficiency multijunction thin-film silicon solar cells," Prog. Photovoltaics: Res. Appl. **23**, 949–963 (2015).
14. H. Sai, T. Matsui, and K. Matsubara, "Stabilized 14.0%-efficient triple-junction thin-film silicon solar cell," Appl. Phys. Lett. **109**, 183506 (2016).
15. S. Hitoshi, M. Takuya, K. Hideo, and M. Koji, "Thin-film microcrystalline silicon solar cells: 11.9% efficiency and beyond," Appl. Phys. Express **11**, 022301 (2018).
16. O. Isabella, J. Krč, and M. Zeman, "Modulated surface textures for enhanced light trapping in thin-film silicon solar cells," Appl. Phys. Lett. **97**, 101106 (2010).
17. L. Tsakalakos, J. Balch, J. Fronheiser, B. A. Korevaar, O. Sulima, and J. Rand, "Silicon nanowire solar cells," Appl. Phys. Lett. **91**, 233117 (2007).
18. B. Tian, X. Zheng, T. J. Kempa, Y. Fang, N. Yu, G. Yu, J. Huang, and C. M. Lieber, "Coaxial silicon nanowires as solar cells and nanoelectronic power sources," Nature **449**, 885–889 (2007).

Optics EXPRESS

19. E. C. Garnett and P. Yang, "Silicon nanowire radial p-n junction solar cells," J. Am. Chem. Soc. **130**, 9224–9225 (2008).
20. J. Zhu, Z. Yu, G. F. Burkhard, C.-M. Hsu, S. T. Connor, Y. Xu, Q. Wang, M. McGehee, S. Fan, and Y. Cui, "Optical absorption enhancement in amorphous silicon nanowire and nanocone arrays," Nano Lett. **9**, 279–282 (2009).
21. C.-M. Hsu, C. Battaglia, C. Pahud, Z. Ruan, F.-J. Haug, S. Fan, C. Ballif, and Y. Cui, "High-efficiency amorphous silicon solar cell on a periodic nanocone back reflector," Adv. Energy Mater. **2**, 628–633 (2012).
22. R.-E. Nowak, M. Vehse, O. Sergeev, T. Voss, M. Seyfried, K. von Maydell, and C. Agert, "Zno nanorods with broadband antireflective properties for improved light management in silicon thin-film solar cells," Adv. Opt. Mater. **2**, 94–99 (2014).
23. L. W. Veldhuizen, Y. Kuang, and R. E. I. Schropp, "Ultrathin tandem solar cells on nanorod morphology with 35-nm thick hydrogenated amorphous silicon germanium bottom cell absorber layer," Sol. Energy Mater. Sol. Cells **158**, 209–213 (2016).
24. O. Isabella, P. Liu, B. Bolman, J. Krč, A. Smets, and M. Zeman, "Modulated surface-textured substrates with high haze: from concept to application in thin-film silicon solar cells," in *Proceedings of the 37th Photovoltaic Specialists Conference (PVSC-37),* (IEEE, 2011), pp. 616–621.
25. C. Battaglia, C.-M. Hsu, K. Söderström, J. Escarré, F.-J. Haug, M. Charrière, M. Boccard, M. Despeisse, D. T. L. Alexander, M. Cantoni, Y. Cui, and C. Ballif, "Light trapping in solar cells: Can periodic beat random?" ACS Nano **6**, 2790–2797 (2012).
26. P. Spinelli, M. A. Verschuuren, and A. Polman, "Broadband omnidirectional antireflection coating based on subwavelength surface mie resonators," Nat. Commun. **3**, 692 (2012).
27. O. Isabella, R. Vismara, A. Ingenito, N. Rezaei, and M. Zeman, "Decoupled front/back dielectric textures for flat ultra-thin c-si solar cells," Opt. Express **24**, A708–A719 (2016).
28. A. Furasova, E. Calabró, E. Lamanna, E. Tiguntseva, E. Ushakova, E. Ubyivovk, V. Mikhailovskii, A. Zakhidov, S. Makarov, and A. Di Carlo, "Resonant silicon nanoparticles for enhanced light harvesting in halide perovskite solar cells," Adv. Opt. Mater. **6**, 1800576 (2018).
29. N. Odebo Länk, R. Verre, P. Johansson, and M. Käll, "Large-scale silicon nanophotonic metasurfaces with polarization independent near-perfect absorption," Nano Lett. **17**, 3054–3060 (2017).
30. V. G. Kravets, F. Schedin, R. Jalil, L. Britnell, R. V. Gorbachev, D. Ansell, B. Thackray, K. S. Novoselov, A. K. Geim, A. V. Kabashin, and A. N. Grigorenko, "Singular phase nano-optics in plasmonic metamaterials for label-free single-molecule detection," Nat. Mater. **12**, 304 (2013).
31. M. Svedendahl, R. Verre, and M. Käll, "Refractometric biosensing based on optical phase flips in sparse and short-range-ordered nanoplasmonic layers," Light. Sci. Appl. **3**, e220 (2014).
32. X. Liu, K. Fan, I. V. Shadrivov, and W. J. Padilla, "Experimental realization of a terahertz all-dielectric metasurface absorber," Opt. Express **25**, 191–201 (2017).
33. S. Zanotto, F. P. Mezzapesa, F. Bianco, G. Biasiol, L. Baldacci, M. S. Vitiello, L. Sorba, R. Colombelli, and A. Tredicucci, "Perfect energy-feeding into strongly coupled systems and interferometric control of polariton absorption," Nat. Phys. **10**, 830 (2014).
34. M. L. Brongersma, Y. Cui, and S. Fan, "Light management for photovoltaics using high-index nanostructures," Nat Mater **13**, 451–460 (2014).
35. Y. Sun, Y. Sun, T. Zhang, G. Chen, F. Zhang, D. Liu, W. Cai, Y. Li, X. Yang, and C. Li, "Complete au@zno core-shell nanoparticles with enhanced plasmonic absorption enabling significantly improved photocatalysis," Nanoscale **8**, 10774–10782 (2016).
36. B. C. P. Sturmberg, T. K. Chong, D.-Y. Choi, T. P. White, L. C. Botten, K. B. Dossou, C. G. Poulton, K. R. Catchpole, R. C. McPhedran, and C. Martijn de Sterke, "Total absorption of visible light in ultrathin weakly absorbing semiconductor gratings," Optica **3**, 556–562 (2016).
37. R. Alaee, M. Albooyeh, and C. Rockstuhl, "Theory of metasurface based perfect absorbers," J. Phys. D: Appl. Phys. **50**, 503002 (2017).
38. M. Boccard, M. Despeisse, J. Escarre, X. Niquille, G. Bugnon, S. HÃđnni, M. Bonnet-Eymard, F. Meillaud, and C. Ballif, "High-stable-efficiency tandem thin-film silicon solar cell with low-refractive-index silicon-oxide interlayer," IEEE J. Photovoltaics **4**, 1368–1373 (2014).
39. S. Hänni, M. Boccard, G. Bugnon, M. Despeisse, J.-W. Schüttauf, F.-J. Haug, F. Meillaud, and C. Ballif, "Microcrystalline silicon solar cells with passivated interfaces for high open-circuit voltage," Phys. Status Solidi A **212**, 840–845 (2015).
40. F.-J. Haug and C. Ballif, "Light management in thin film silicon solar cells," Energy Environ. Sci. **8**, 824–837 (2015).
41. S. W. Glunz and F. Feldmann, "SiO_2 surface passivation layers – a key technology for silicon solar cells," Sol. Energy Mater. Sol. Cells **185**, 260–269 (2018).
42. "Lumerical fdtd solutions," http://www.lumerical.com/products/fdtd-solutions/. Accessed: 2018-22-11.
43. P. B. Johnson and R. W. Christy, "Optical constants of the noble metals," Phys. Rev. B **6**, 4370–4379 (1972).
44. P. Grahn, A. Shevchenko, and M. Kaivola, "Electromagnetic multipole theory for optical nanomaterials," New J. Phys. **14**, 093033 (2012).
45. "Ansys hfss white papers," http://www.ansys.com/Products/Electronics/ANSYS-HFSS. Accessed: 2018-09-11.

Optics EXPRESS

46. R. Vismara, O. Isabella, and M. Zeman, "Back-contacted $BaSi_2$ solar cells: an optical study," Opt. Express **25**, A402–A408 (2017).
47. O. Isabella, R. Vismara, D. N. P. Linssen, K. X. Wang, S. Fan, and M. Zeman, "Advanced light trapping scheme in decoupled front and rear textured thin-film silicon solar cells," Sol. Energy **162**, 344–356 (2018).
48. O. Isabella, H. Sai, M. Kondo, and M. Zeman, "Full-wave optoelectrical modeling of optimized flattened light-scattering substrate for high efficiency thin-film silicon solar cells," Prog. Photovoltaics: Res. Appl. **22**, 671–689 (2014).
49. C. Onwudinanti, R. Vismara, O. Isabella, L. Grenet, F. Emieux, and M. Zeman, "Advanced light management based on periodic textures for cu(in,ga)se2 thin-film solar cells," Opt. Express **24**, A693–A707 (2016).
50. NREL, "Reference solar spectral irradiance: Air mass 1.5," https://rredc.nrel.gov/solar//spectra/am1.5/. Accessed 2019-02-25.
51. W. W. Salisbury, "Absorbent body for electromagnetic waves," (1952). US Patent No. 2,599,944.
52. T. Koida, H. Fujiwara, and M. Kondo, "Hydrogen-doped In_2O_3 as high-mobility transparent conductive oxide," Jpn. J. Appl. Phys. **46**, L685 (2007).
53. T. Koida, H. Fujiwara, and M. Kondo, "Reduction of optical loss in hydrogenated amorphous silicon/crystalline silicon heterojunction solar cells by high-mobility hydrogen-doped In_2O_3 transparent conductive oxide," Appl. Phys. Express **1**, 041501 (2008).
54. H. Fujiwara and M. Kondo, "Effects of carrier concentration on the dielectric function of zno:ga and in_2o_3 : Sn studied by spectroscopic ellipsometry: Analysis of free-carrier and band-edge absorption," Phys. Rev. B **71**, 075109 (2005).
55. J. Springer, A. Poruba, L. Müllerova, M. Vanecek, O. Kluth, and B. Rech, "Absorption loss at nanorough silver back reflector of thin-film silicon solar cells," J. Appl. Phys. **95**, 1427–1429 (2004).
56. F.-J. Haug, T. Söderström, O. Cubero, V. Terrazzoni-Daudrix, and C. Ballif, "Influence of the zno buffer on the guided mode structure in si/zno/ag multilayers," J. Appl. Phys. **106**, 044502 (2009).
57. H. Tan, R. Santbergen, A. H. Smets, and M. Zeman, "Plasmonic light trapping in thin-film silicon solar cells with improved self-assembled silver nanoparticles," Nano Lett. **12**, 4070–4076 (2012).
58. G. Yang, "High-efficient n-i-p thin-film silicon solar cells," Ph.D. thesis, Delft University of Technology (2015).
59. R. Verre, N. Odebo Länk, D. Andrén, H. Šípová, and M. Käll, "Large-scale fabrication of shaped high index dielectric nanoparticles on a substrate and in solution," Adv. Opt. Mater. **6**, 1701253 (2018).
60. P. Krogstrup, H. I. Jorgensen, M. Heiss, O. Demichel, J. V. Holm, M. Aagesen, J. Nygard, and A. Fontcuberta i Morral, "Single-nanowire solar cells beyond the shockley-queisser limit," Nat Photon **7**, 306–310 (2013).
61. S. Liu, M. B. Sinclair, S. Saravi, G. A. Keeler, Y. Yang, J. Reno, G. M. Peake, F. Setzpfandt, I. Staude, T. Pertsch, and I. Brener, "Resonantly enhanced second-harmonic generation using iiiâĂŞv semiconductor all-dielectric metasurfaces," Nano Lett. **16**, 5426–5432 (2016).
62. R. Camacho-Morales, M. Rahmani, S. Kruk, L. Wang, L. Xu, D. A. Smirnova, A. S. Solntsev, A. Miroshnichenko, H. H. Tan, F. Karouta, S. Naureen, K. Vora, L. Carletti, C. De Angelis, C. Jagadish, Y. S. Kivshar, and D. N. Neshev, "Nonlinear generation of vector beams from algaas nanoantennas," Nano Lett. **16**, 7191–7197 (2016).
63. E. Y. Tiguntseva, G. P. Zograf, F. E. Komissarenko, D. A. Zuev, A. A. Zakhidov, S. V. Makarov, and Y. S. Kivshar, "Light-emitting halide perovskite nanoantennas," Nano Lett. **18**, 1185–1190 (2018).
64. S. V. Makarov, V. Milichko, E. V. Ushakova, M. Omelyanovich, A. Cerdan Pasaran, R. Haroldson, B. Balachandran, H. Wang, W. Hu, Y. S. Kivshar, and A. A. Zakhidov, "Multifold emission enhancement in nanoimprinted hybrid perovskite metasurfaces," ACS Photonics **4**, 728–735 (2017).
65. G. E. Jellison, "Optical functions of gaas, gap, and ge determined by two-channel polarization modulation ellipsometry," Opt. Mater. **1**, 151–160 (1992).
66. P. Löper, M. Stuckelberger, B. Niesen, J. Werner, M. Filipič, S.-J. Moon, J.-H. Yum, M. Topič, S. De Wolf, and C. Ballif, "Complex refractive index spectra of $CH_3NH_3PbI_3$ perovskite thin films determined by spectroscopic ellipsometry and spectrophotometry," J. Phys. Chem. Lett. **6**, 66–71 (2015).
67. A. E. Miroshnichenko, A. B. Evlyukhin, Y. F. Yu, R. M. Bakker, A. Chipouline, A. I. Kuznetsov, B. Luk'yanchuk, B. N. Chichkov, and Y. S. Kivshar, "Nonradiating anapole modes in dielectric nanoparticles," Nat. Commun. **6**, 8069 (2015).
68. A. Kodigala, T. Lepetit, Q. Gu, B. Bahari, Y. Fainman, and B. Kanté, "Lasing action from photonic bound states in continuum," Nature **541**, 196 (2017).